npj Computational Materials

www.nature.com/npjcompumats

ARTICLE OPEN

# Prediction of room-temperature half-metallicity in layered halide double perovskites

Jian Xu[1,2], Changsong Xu[3], Jian-Bo Liu[1*], Laurent Bellaiche[3], Hongjun Xiang[4], Bai-Xin Liu[1] and Bing Huang[2*]

Half-metallic ferromagnets (HMFs) that possess intriguing physical properties with completely spin-polarized current are key candidates for high-efficiency spintronic devices. However, HMFs that could simultaneously have high Curie temperature ($T_c$), wide half-metallic gap ($\Delta_{HM}$), and large bulk magnetocrystalline anisotropy energy (MAE) are very rare, which significantly restrict their room-temperature (RT) applications. In this article, through materials screening in layered halide double perovskites (LHDPs), we have theoretically identified that $Cs_4FePb_2Cl_{12}$, which has good crystallographic, dynamic and thermal stabilities, possesses an intrinsic half-metallic ground-state with a high $T_c$ ~ 450 K. Interestingly, the long-range ferromagnetic ordering in bulk $Cs_4FePb_2Cl_{12}$ is contributed by the strong super-superexchange interactions between the neighboring Fe *d* orbitals mediated by different anionic Cl *p* orbitals. The high $T_c$ of layered $Cs_4FePb_2Cl_{12}$ can be well maintained even in the monolayer limitation, i.e., $T_c$ ~ 370 K for $Cs_4FePb_2Cl_{12}$ monolayer, which is critical for nanoscale device applications. Moreover, both bulk and monolayer $Cs_4FePb_2Cl_{12}$ can exhibit wide $\Delta_{HM}$ ~ 0.55 eV and large MAE >320 μeV/Fe, comparable to that of the best HMFs reported in the literature. Our findings can significantly extend the potentials of LHDPs for high-temperature spintronic applications.

*npj Computational Materials* (2019)5:114 ; https://doi.org/10.1038/s41524-019-0252-6

## INTRODUCTION

Half-metallic ferromagnets (HMFs), coexisting metallic nature for electrons in one spin channel and insulating nature in the other, can generate completely spin-polarized electrical current, and are considered as key candidates for many spintronic applications from magnetic memories to spin-polarized tunneling devices.[1–3] In order to develop high-performance spintronic devices, three criteria are highly required for a HMF: (1) a high Curie temperature ($T_c$) for room-temperature (RT) applications, (2) a wide half-metallic gap ($\Delta_{HM}$) to efficiently prevent the spin-flip transition of carriers due to thermal excitation, and (3) a large bulk magnetocrystalline anisotropy energy (MAE) to overcome the thermal-fluctuation-induced random and uncontrollable switching of spins.[4] Although some HMFs have been reported theoretically and experimentally,[2,3,5–8] to our knowledge, most of them cannot fulfill all these criteria.

Inorganic metal halide perovskites, which are advantaged in their exceptional defect tolerance, low-cost solution processing and tunable emission across the visible spectrum, have multiple optoelectronic applications, e.g., solar cells, photodetectors, light-emitting diodes, transparent conductors, transistors, and lasing applications.[9–22] Very recently, a new type of ⟨111⟩-oriented layered halide double perovskite (LHDP), e.g., $Cs_4CuSb_2Cl_{12}$ and $Cs_4MnSb_2Cl_{12}$, have been synthesized successfully in experiments with good tolerance towards humidity, heat and light.[23–26] Interestingly, it is found that $Cs_4MnSb_2Cl_{12}$ exhibits weak antiferromagnetic (AFM) ordering between the first nearest-neighboring (NN) Mn ions. The observation of AFM ground-state in $Cs_4MnSb_2Cl_{12}$ opens up new possibilities in discovering ferromagnetic (FM) ordering, even half-metallicity, in LHDPs.

In this article, we have explored the possibility of the existence of half-metallicity in LHDPs using first-principles calculations based computational material screening in a large number of LHDPs with the stoichiometries of $Cs_4MB_2X_{12}$ ($Cs_4M^{2+}B^{3+}{}_2X^{VII}{}_{12}$ and $Cs_4M^{4+}B^{2+}{}_2X^{VII}{}_{12}$). Among several compounds that have good dynamic and thermal stabilities, interestingly, we identify that the $Cs_4FePb_2Cl_{12}$ can exhibit a half-metallic ground-state with a calculated $T_c$ above RT ($T_c$ ~ 450 K). Meanwhile, $Cs_4FePb_2Cl_{12}$ has a wide $\Delta_{HM}$ ~ 0.55 eV and a large MAE ~ 380 μeV/Fe, which ranks $Cs_4FePb_2Cl_{12}$ as one of the best half-metallic materials for spintronics. Remarkably, when the thickness of layered $Cs_4FePb_2Cl_{12}$ is reduced to monolayer, it can still sustain the half-metallicity with a high $T_c$ ~ 370 K and a strong MAE ~ 318 μeV/Fe. The external strain can be applied to efficiently manipulate the magnetic coupling and MAE of $Cs_4FePb_2Cl_{12}$.

## RESULTS AND DISCUSSION

The family of $Cs_4MB_2X_{12}$ ($Cs_4M^{2+}B^{3+}{}_2X^{VII}{}_{12}$ or $Cs_4M^{4+}B^{2+}{}_2X^{VII}{}_{12}$) is a unique mixed metal ⟨111⟩-oriented layered perovskite with each B-M-B layer consisting of three sublayers (one M octahedral layer and two B octahedral layers) (see Fig. 1a). The inclusion of Cs is very critical to stabilize the perovskite structure.[27] Since the distances between two NN M ions are quite large (>7 Å) in $Cs_4MB_2X_{12}$ family LHDPs, the direct exchange coupling between them is extremely weak.[28–30] Instead, from the orbital-projected density of states (DOS), we can find that a strong coupling between M *d* and X *p* orbitals generally exists in $Cs_4MB_2X_{12}$ (Supplementary Fig. 1). The two NN M ions could interact with each other through the bridging $BX_6$ octahedron via super-superexchange mechanism, as shown in Fig. 1b.

### Origin of AFM ground-state in $Cs_4MnSb_2Cl_{12}$

To explore how to achieve FM in LHDPs, first, we bring the origin of the AFM behavior in $Cs_4Mn^{2+}Sb^{3+}{}_2Cl_{12}$ LHDP, as observed in

[1]Key Laboratory of Advanced Materials (MOE), School of Materials Science and Engineering, Tsinghua University, Beijing 100084, China. [2]Beijing Computational Science Research Center, Beijing 100193, China. [3]Physics Department and Institute for Nanoscience and Engineering, University of Arkansas, Fayetteville, AR 72701, USA. [4]Key Laboratory of Computational Physical Sciences (Ministry of Education), State Key Laboratory of Surface Physics, and Department of Physics, Fudan University, Shanghai 200433, China. *email: jbliu@mail.tsinghua.edu.cn; bing.huang@csrc.ac.cn

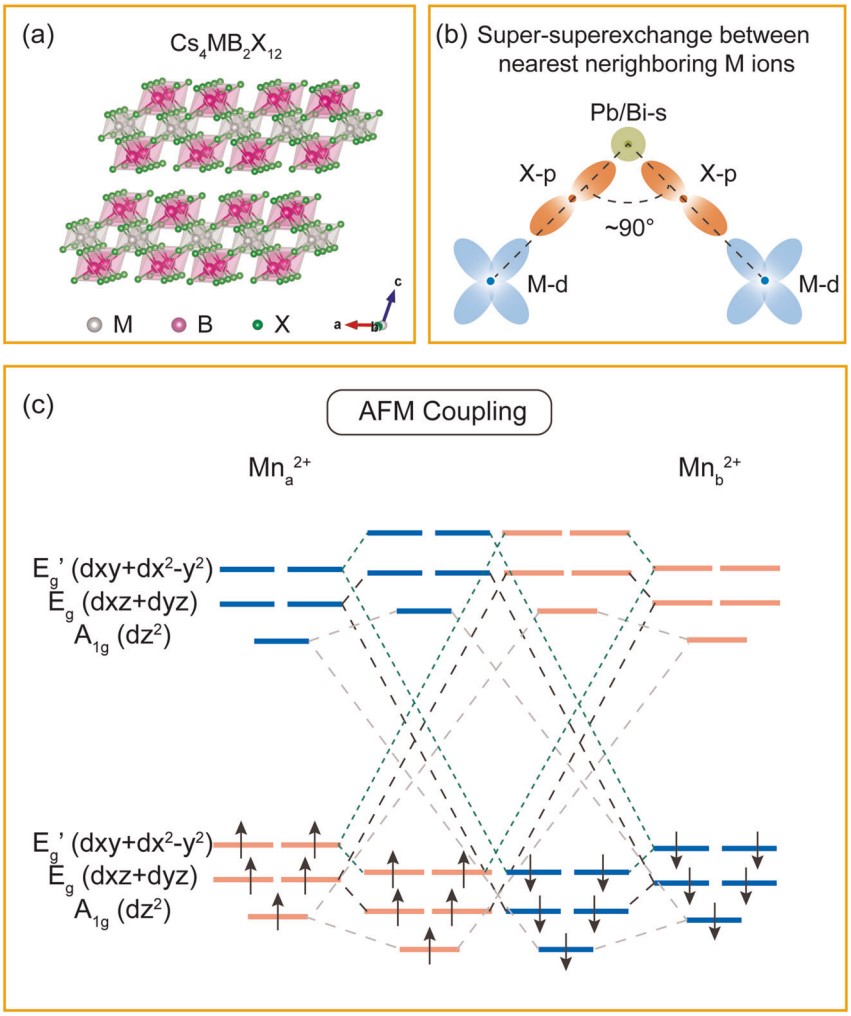


**Fig. 1** Magnetic mechanism. **a** Crystal structure of $Cs_4MB_2X_{12}$ LHDP. Voids between the octahedrons are filled with Cs atoms, which are omitted for clarity. **b** Schematic diagram of the super-superexchange interaction in $Cs_4MB_2X_{12}$ LHDPs. **c** Schematic diagram of AFM coupling in experimental synthesized $Cs_4MnSb_2Cl_{12}$. Red and blue bars represent spin-up and spin-down states, respectively.

recent experiment,[24] to light. Based on the crystal field theory, the five *d* orbitals of Mn will split into a singlet $A_{1g}$ $(d_{z^2})$, doublet $E_g$ $(d_{xz}+d_{yz})$, and doublet $E_g'$ $(d_{xy}+d_{x^2-y^2})$ orbitals under a $D_{3d}$ crystal symmetry. The order of *d*-orbital energies ($A_{1g}$, $E_g$, $E_g'$) is determined by the interaction strength of X *p* orbital and M *d* orbital.[31] Moreover, it is found that the $Mn^{2+}$ in $Cs_4MnSb_2Cl_{12}$ favors a high spin configuration of $d^5\uparrow d^0\downarrow$, resulting in the magnetic moments of 5 $\mu_B$/Mn. As shown in Fig. 1c, the orbital coupling between the two NN Mn ions, i.e., $Mn_a^{2+}$ and $Mn_b^{2+}$, can gain energy only if they have antiparallel spin alignment (AFM coupling). For example, the interaction between the occupied $Mn_a^{2+}-E_g'\uparrow$ and empty $Mn_b^{2+}-E_g'\uparrow$ would lead to a doublet low-lying bonding states and another doublet high-lying antibonding states. A similar orbital coupling occurs between the occupied $Mn_b^{2+}-E_g'\downarrow$ and empty $Mn_a^{2+}-E_g'\downarrow$. Finally, the five electrons would occupy five low-lying bonding states to maximize the energy gain of the system. As demonstrated in $Cs_4MnSb_2Cl_{12}$, the magnetic ground-states in $Cs_4MB_2X_{12}$ are mainly determined by the orbital occupations of M ions via super-superexchange interactions. Therefore, it is interesting to further explore the possibility of the existence of long-range FM ordering in a large number of unknown $Cs_4MB_2X_{12}$ LHDPs.

## Materials screening for stable $Cs_4MB_2X_{12}$ compounds

We have considered the combinations of (Cs, $M^{2+}$, $B^{3+}$, $X^{VII}$) with $M^{2+}=Ti^{2+}/V^{2+}/Cr^{2+}/Mn^{2+}/Fe^{2+}/Co^{2+}/Ni^{2+}/Cu^{2+}$, $B^{3+}=Sb^{3+}/In^{3+}/Bi^{3+}$, and $X^{VII}=Cl^-/Br^-/I^-$ in $Cs_4M^{2+}B^{3+}{}_2X^{VII}{}_{12}$ LHDPs and (Cs, $M^{4+}$, $B^{2+}$, $X^{VII}$) with $M^{2+}=Ti^{2+}/V^{2+}/Cr^{2+}/Mn^{2+}/Fe^{2+}/Co^{2+}/Ni^{2+}$, $B^{2+}=Pb^{2+}/Ge^{2+}$, and $X^{VII}=Cl^-/Br^-/I^-$ in $Cs_4M^{4+}B^{2+}{}_2X^{VII}{}_{12}$ LHDPs (see Fig. 2a). In order to discover possible promising magnets for spintronics in unknown $Cs_4MB_2X_{12}$ compounds, material stability is an important issue to be clarified (Fig. 2b). Firstly, to evaluate the crystallographic stability of materials in the perovskite structure, Goldschmidt's empirical criterion is adopted with two empirical quantities: the Goldschmidt tolerance factor (*t*) and the octahedral factor ($\mu$).[27,32–34] It is found that the formation of stable perovskite structures requires $0.81<t<1.11$ and $0.41<\mu<0.90$.[27,32] Among all the 114 compounds, we found that 57 of them fall into the empirical stable areas of perovskite structures (Supplementary Note 1 and Supplementary Fig. 2).

Secondly, to evaluate the thermodynamic stabilities of the above 57 $Cs_4MB_2X_{12}$ compounds, we calculate their decomposition enthalpies (ΔH) with respect to possible decomposition pathways involving all the existing binary and ternary secondary phases from the Inorganic Crystal Structure Database (ICSD)[35] and Automatic Flow (AFLOW).[36] Besides of the existing $Cs_4CuSb_2Cl_{12}$,

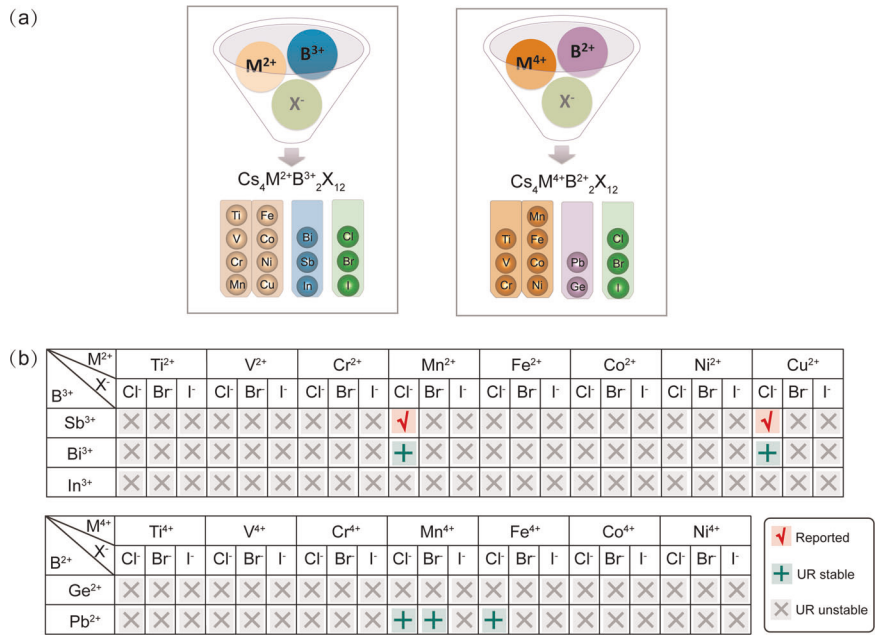


**Fig. 2** Materials design strategy and materials screening. **a** Schematic diagram of the formation of $Cs_4MB_2X_{12}$ ($Cs_4M^{2+}B^{3+}{}_2X^{VII}{}_{12}$ and $Cs_4M^{4+}B^{2+}{}_2X^{VII}{}_{12}$) LHDPs with different components. **b** Predicting stable $Cs_4M^{2+}B^{3+}{}_2X^{VII}{}_{12}$ and $Cs_4M^{4+}B^{2+}{}_2X^{VII}{}_{12}$ compounds. The "red check" indicates the compounds that have been synthesized in experiments, whereas the "green plus" and "gray cross" mean these compounds that are unreported (UR) in literatures.

$Cs_4MnSb_2Cl_{12}$, we found that there are another eight compounds ($Cs_4MnBi_2Cl_{12}$, $Cs_4CuBi_2Cl_{12}$, $Cs_4CuIn_2Cl_{12}$, $Cs_4MnPb_2Cl_{12}$, $Cs_4FePb_2Cl_{12}$, $Cs_4NiPb_2Cl_{12}$, $Cs_4MnPb_2Br_{12}$, and $Cs_4NiPb_2Br_{12}$) exhibiting good thermodynamic stabilities with positive ΔH (Supplementary Note 2 and Supplementary Fig. 3). Finally, we have confirmed their dynamical and thermal stabilities. It is found that except for $Cs_4CuIn_2Cl_{12}$, $Cs_4NiPb_2Cl_{12}$, and $Cs_4NiPb_2Br_{12}$, the other five compounds exhibit good phonon stability evidenced by no imaginary modes in the whole Brillouin zone (Supplementary Fig. 4) and thermally dynamical stability at RT evidenced by the ab initio molecular dynamic (AIMD) simulations (Supplementary Fig. 5).

## Origin of FM ground-state in $Cs_4FePb_2Cl_{12}$

For the stable $Cs_4MB_2X_{12}$ compounds, we have explored all the possible magnetic configurations, including one FM configuration, three collinear antiferromagnetic order (AFM-I, AFM-II, and AFM-III) and non-collinear antiferromagnetic order (AFM-N), as shown in Fig. 3a. In AFM-I configuration, each M-B-M layer is ferromagnetic, but antiferromagnetic with respect to its neighboring M-B-M layers. For AFM-II configuration, each [$MX_6$] along the [010] direction is ferromagnetic but with antiferromagnetic coupling to its neighboring [$MX_6$]. For AFM-III configuration, each [$MX_6$] along the [010] direction is antiferromagnetic.[37] In AFM-N configuration, the spin directions on the three NN M atoms lie 120 degrees apart in space, and each M atom has the same magnetic moment, resulting in zero net magnetization in the system. After the total energy calculations, we find that the magnetic ground-states of all the stable $Cs_4MB_2X_{12}$ are AFM, except for $Cs_4FePb_2Cl_{12}$ (Fig. 3b and Supplementary Note 3).

As shown in Fig. 3c, in $Cs_4MnBi_2Cl_{12}$, $Cs_4CuBi_2Cl_{12}$, $Cs_4MnPb_2Cl_{12}$, $Cs_4MnPb_2Br_{12}$, and $Cs_4FePb_2Cl_{12}$, the M atoms favor high spin configurations of $d^5\uparrow d^0\downarrow$, $d^5\uparrow d^4\downarrow$, $d^3\uparrow d^0\downarrow$, $d^3\uparrow d^0\downarrow$, and $d^4\uparrow d^0\downarrow$, respectively. Interestingly, it is found that the local magnetic moments in $Cs_4MnBi_2Cl_{12}$, $Cs_4CuBi_2Cl_{12}$, $Cs_4MnPb_2Cl_{12}$, and $Cs_4MnPb_2Br_{12}$ are contributed by fully-filled M *d* orbitals. Similar to the case of $Cs_4MnSb_2Cl_{12}$, the existence of AFM ground-states in these four $Cs_4MB_2X_{12}$ can be well understood. While in $Cs_4FePb_2Cl_{12}$ with a local magnetic moment contributed by a half-filled Fe *d* orbital, when the NN $Fe_a^{4+}$ and $Fe_b^{4+}$ have the same spin alignment (FM coupling), the interaction between the half-filled $Fe_a^{4+}$ and the half-filled $Fe_b^{4+}$ would result in an energy lowering (Fig. 3d). Therefore, the magnetic ground-state of $Cs_4FePb_2Cl_{12}$ could be a FM phase.

## Electronic and magnetic properties of $Cs_4FePb_2Cl_{12}$

We now look into the electronic properties of $Cs_4FePb_2Cl_{12}$. As shown in Fig. 4 and Supplementary Fig. 7, interestingly, we find that $Cs_4FePb_2Cl_{12}$ is a HMF with 100% spin-polarized conduction electrons near the Fermi level irrespective of the spin-orbit coupling (SOC). We also confirm that $Cs_4FePb_2Cl_{12}$ remains half-metallic by using the PBE+U method.[38] The $\Delta_{HM}$, which is defined as the minimum of the bottom energy of minority spin conduction bands with respect to the Fermi level and the absolute values of the top energy of minority spin valence bands,[39,40] is estimated to be 0.55 eV in $Cs_4FePb_2Cl_{12}$. The value of $\Delta_{HM}$ in $Cs_4FePb_2Cl_{12}$ is among one of the best values reported in other intrinsic HMFs, e.g., quaternary Heusler alloys CoFeCrAl and CoFeCrSi (0.16 and 0.28 eV),[41,42] double perovskites $Sr_2FeMoO_6$ (~0.5 eV),[6] and zincblende phases of the transition metal chalcogenides CrTe, CrSe, and VTe (<0.60 eV).[7,40] A wide $\Delta_{HM}$ can efficiently prevent the spin-flip transition of carriers due to thermal excitation and thus enhance the stability of its half-metallicity.

From the spin densities (Fig. 4c), it is seen that only Fe *d* orbitals contribute to the magnetism of $Cs_4FePb_2Cl_{12}$. To further confirm the electronic stability of $Cs_4FePb_2Cl_{12}$ at finite temperature, an AIMD simulation on $Cs_4FePb_2Cl_{12}$ is performed at 300 K. As shown in Fig. 4d, under thermal fluctuations, the FM ground-state can be well maintained at 300 K after 1 ps. The oscillation of $\Delta_{HM}$ values at 300 K is in the range of 0.46–0.61 eV (Fig. 4e), which is large enough for RT applications.

To develop practical spintronic applications, the magnetic properties of the compounds at finite temperatures should be explored. We adopt the following classical Heisenberg

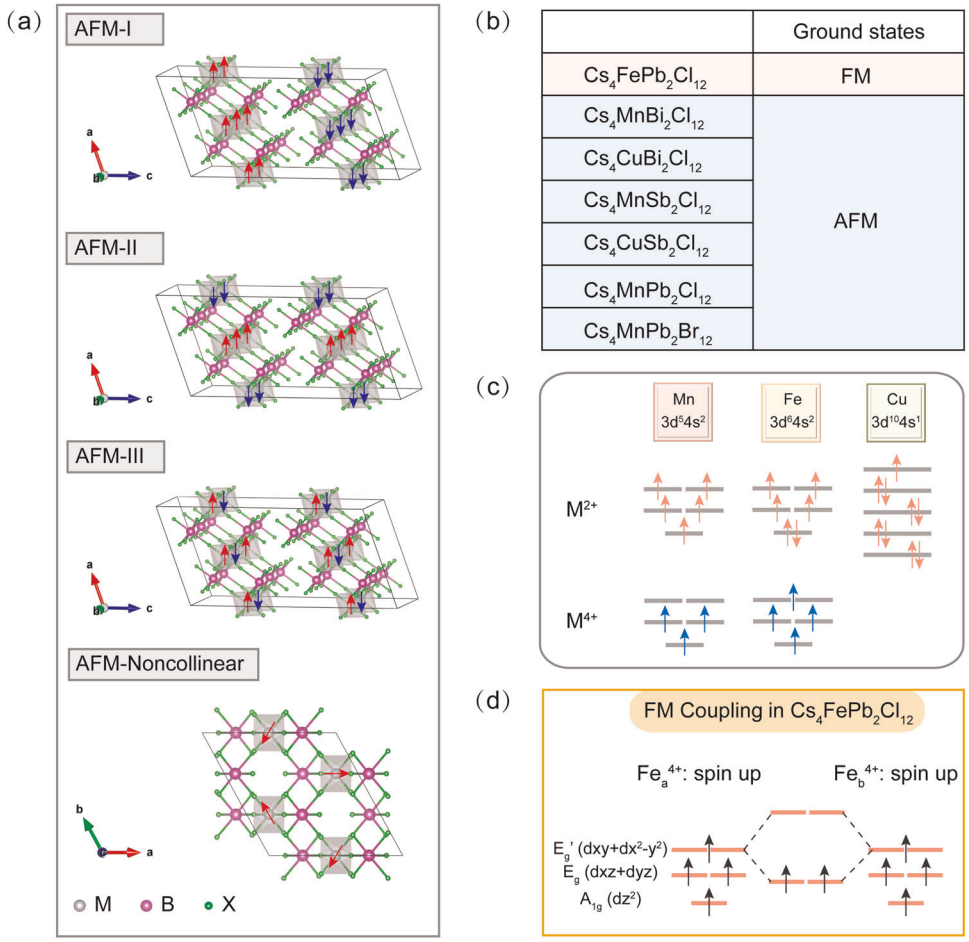


**Fig. 3** Magnetic ground-states of stable compounds. **a** A $Cs_4MB_2X_{12}$ with different AFM configurations. Voids between the octahedrons are filled with Cs atoms, which are omitted for clarity. Arrows denote the spin directions. **b** Magnetic ground-states for the seven stable $Cs_4MB_2X_{12}$ compounds. **c** Schematic diagram of electron occupation of $M^{2+}$ in $Cs_4M^{2+}Bi_2Cl_{12}$ ($M^{2+} = Mn^{2+}/Fe^{2+}/Cu^{2+}$) and $M^{4+}$ in $Cs_4M^{4+}Pb_2Cl_{12}$ ($M^{2+} = Mn^{2+}/Fe^{2+}$). **d** Schematic diagram of FM coupling in $Cs_4FePb_2Cl_{12}$.

Hamiltonian:

$$H = -\sum_{<i,j>} J_1 S_i \cdot S_j - \sum_{<k,l>} J_2 S_k \cdot S_l - \sum_{<m,n>} J_3 S_m \cdot S_n - \sum_{<i>} D(S_{iz})^2$$

where $J_1$, $J_2$, and $J_3$ are the first, second and third nearest-neighbor magnetic exchange parameters, respectively. $S_{i\ (j,k,l,m,n)}$ is the spin magnetic moment on the magnetic atom at site *i* (*j*, *k*, *l*, *m*, *n*). *D* is the single-site magnetic anisotropy parameter, and $S_{iz}$ represent components of **S** along *z* (out-of-plane) orientations. The positive and negative *J* (*D*) values represent FM coupling (out-of-plane easy axis) and AFM couplings (in-plane easy axis), respectively. The calculated $J_1$, $J_2$, and $J_3$ of $Cs_4FePb_2Cl_{12}$ are $J_1 = 5.1$ meV, $J_2 = 1.3$ meV, and $J_3 = 0.6$ meV. Interestingly, the interlayer exchange interaction ($J_3$) is much weaker than the intralayer interaction ($J_1$ and $J_2$), due to the large vdW interlayer distance.

Based on Monte Carlo (MC) simulations,[43] the $T_c$ of $Cs_4FePb_2Cl_{12}$ is estimated to be 442 K (Fig. 5d), which is well above RT and among the highest $T_c$ of intrinsic HMFs reported in the literatures.[8,44–46] As a benchmark, the Neel temperature of $Cs_4MnSb_2Cl_{12}$ (AFM ground-state) is calculated to be ~1 K, which is consistent with the experimental measurements[24] and thus testify the accuracy of our calculations.

As for a layered structure, it is interesting to further understand the electronic and magnetic properties of monolayer $Cs_4FePb_2Cl_{12}$ (Fig. 5a). As shown in Fig. 5b, the exfoliation energy ($E_{xf}$) of $Cs_4FePb_2Cl_{12}$, i.e., the energy required to separate an individual layer from the bulk compound to infinity, is calculated to be 0.16 J/m$^2$, which is comparable to that for a large number of layered compounds (around 0.32 J/m$^2$).[47,48] It indicates that $Cs_4FePb_2Cl_{12}$ monolayer might be exfoliated from bulk $Cs_4FePb_2Cl_{12}$, once bulk $Cs_4FePb_2Cl_{12}$ can be synthesized in the experiments.

As shown in Fig. 5c, $Cs_4FePb_2Cl_{12}$ monolayer remains half-metallicity with $\Delta_{HM} \sim 0.56$ eV. Most importantly, the $T_c$ of $Cs_4FePb_2Cl_{12}$ monolayer can sustain around RT (370 K), as shown in Fig. 5d, which is a novel advantage over many other magnetic 2D materials. For example, the $T_c$ of $Fe_3GeTe_2$ with a FM ground-state is dramatically reduced from 180 K (in the 3D bulk) to 20 K (in a monolayer).[49] The reduction in the $T_c$ as the samples are thinned down can be explained by the thermal fluctuations of spin waves, whose energy distribution is intimately connected to the dimensionality.[50,51] However, for $Cs_4FePb_2Cl_{12}$, the interlayer exchange interactions ($J_3$) is already weak in the bulk due to the large vdW interlayer distance, and the intralayer exchange interactions ($J_1$ and $J_2$) in the monolayer remain strong enough as that in the bulk. Therefore, the $T_c$ only slightly decreases from 442 K in the bulk to 370 K in the monolayer.

Besides of $\Delta_{HM}$ and $T_c$, we also investigate another important property for spintronic materials, which is related to MAE. From the spatial dependence of the MAE for $Cs_4FePb_2Cl_{12}$ (Fig. 6a), it is found that $Cs_4FePb_2Cl_{12}$ can exhibit an in-plane easy axis and the hardest axis of magnetization (largest MAE value) aligns along the out-of-plane direction. Within the framework of second order perturbation theory, the value of MAE scales with the square of the SOC scaling parameter.[52,53] Thus, the compounds containing

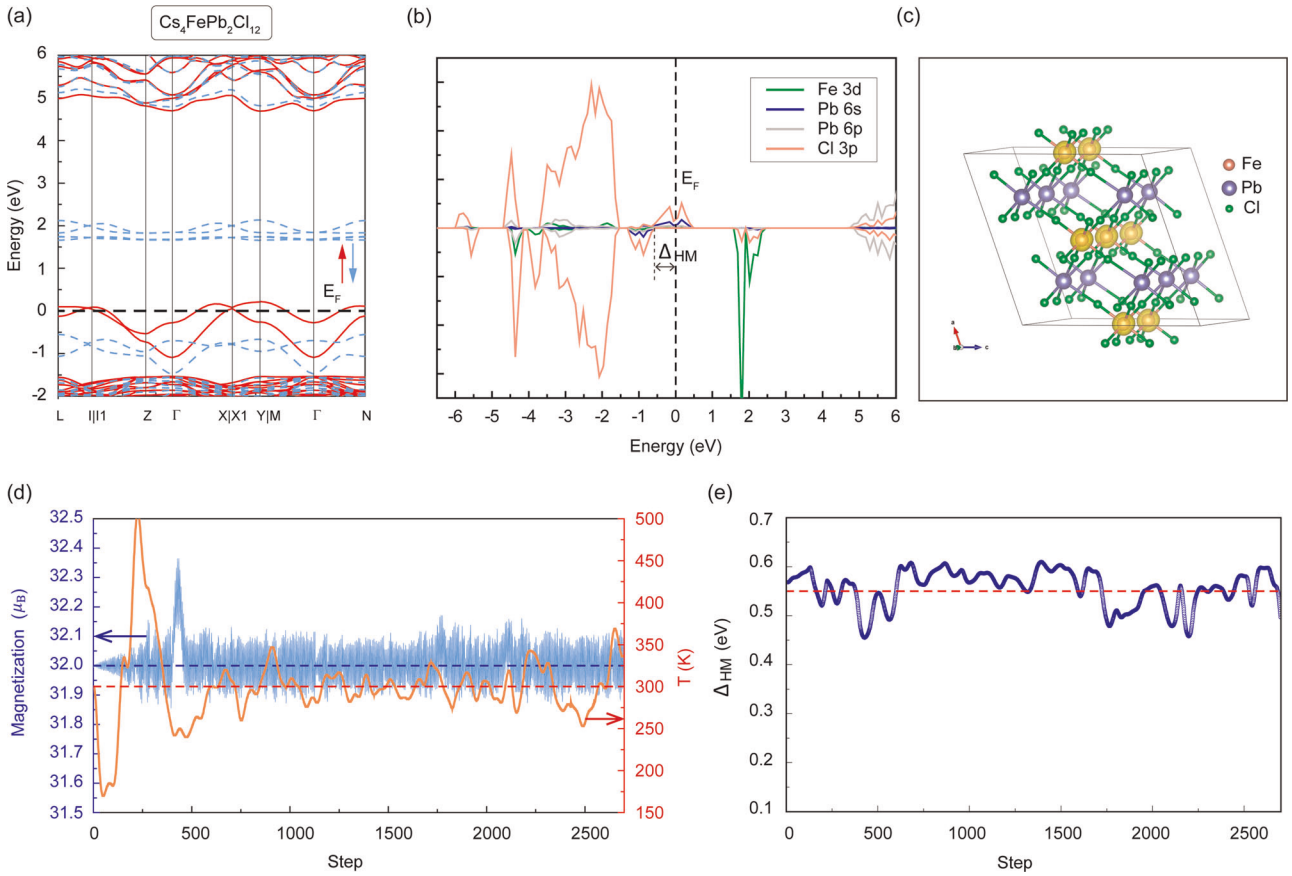


**Fig. 4** Electronic properties of $Cs_4FePb_2Cl_{12}$. **a** Calculated band structure and **b** orbital-projected DOS for $Cs_4FePb_2Cl_{12}$. δ is the half-metallic gap. Fermi level ($E_f$) is set to zero. **c** Spin density of $Cs_4FePb_2Cl_{12}$. Voids between the octahedrons are filled with Cs atoms, which are omitted for clarity. **d** Temperature, magnetization, and **e** $\Delta_{HM}$ as functions of time-steps in AIMD simulation at targeted 300 K for $Cs_4FePb_2Cl_{12}$. The AIMD simulation is performed by using a supercell containing 8 unit cells. The red dashed line in (**e**) shows the $\Delta_{HM}$ value at 0 K.

the heavy elements which have significant SOC effect are expected to have large MAE. The calculated MAE is 380 μeV/Fe for $Cs_4FePb_2Cl_{12}$, which is comparable to or even larger than that in Fe (−1.4 μeV per atom), Co (−65 μeV per atom), Ni (2.7 μeV per atom) bulks,[54] and monolayer of Fe, Co deposited on substrates (80–370 μeV per metal atom).[55,56] The large MAE in bulk $Cs_4FePb_2Cl_{12}$ may be due to the significant SOC effect of Pb element and large structural anisotropy. The large bulk MAE makes $Cs_4FePb_2Cl_{12}$ promising for magneto-electronic applications, and is expected to stabilize the long-range FM order in its 2D systems, which is consistent with our above discussions.

We also studied the strain effect on the magnetic properties of $Cs_4FePb_2Cl_{12}$ monolayer. As shown in Fig. 6c, it is found that the FM configuration is more stable than the AFM configuration within a large range of strain ($-4\% < \varepsilon < 4\%$). From the orbital-projected DOS (Fig. 5c), it can be seen that a pronounced hole state which is mainly formed by Fe 3*d* orbitals with hybridization with Cl 3*p* orbitals, located at 1.8 eV in the spin-down channel. This hole state, which is responsible for the FM ordering, is robust under strains. The FM coupling in the super-superexchange mechanism can be efficiently enhanced under compressive strain, and thus $T_c$ of $Cs_4FePb_2Cl_{12}$ monolayer can be dramatically increased to 448 K under $\varepsilon = -4\%$ (Fig. 6c and Supplementary Fig. 8). From Fig. 6b, it is found that $Cs_4FePb_2Cl_{12}$ exhibits an in-plane easy axis (direction [010] in Fig. 5a). The hardest axis of magnetization aligns along the out-of-plane direction (direction [001] in Fig. 5a). The calculated MAE is 318 μeV/Fe for $Cs_4FePb_2Cl_{12}$ monolayer. The value can be modulated from 215 μeV/Fe under $\varepsilon = -4\%$ to 350 μeV/Fe under $\varepsilon = 4\%$ (Fig. 6d). These MAE values are all large enough for the stability of long-range FM ordering in $Cs_4FePb_2Cl_{12}$ monolayer.

In conclusion, through materials screening by using first-principles calculations, we have identified that $Cs_4FePb_2Cl_{12}$ can exhibit a half-metallic ground-state with high $T_c$, wide $\Delta_{HM}$ and large MAE, which make $Cs_4FePb_2Cl_{12}$ as one of the best HMFs. Further experimental efforts are called for to synthesize this compound. Interestingly, the high $T_c$ of layered $Cs_4FePb_2Cl_{12}$ can be well maintained in $Cs_4FePb_2Cl_{12}$ monolayer. The discovery of $Cs_4FePb_2Cl_{12}$ monolayer can enrich the 2D magnets family, and this material is expected to have applications from sensing to data storage.

## METHODS

### First-principles calculations

First-principles calculations were based on density functional theory (DFT) implemented in the Vienna Ab initio Simulation Package (VASP).[57] The exchange-correlation functional was treated with the generalized gradient approximation (GGA) in the Perdew–Burke–Ernzerhof (PBE) form.[58] To properly describe the strongly correlated electrons in the partially filled *d* subshells in $Cs_4M^{2+}B^{3+}{}_2X^{VII}{}_{12}$ ($M^{2+} = Ti^{2+}/V^{2+}/Cr^{2+}/Mn^{2+}/Fe^{2+}/Co^{2+}/Ni^{2+}/Cu^{2+}$, $B^{3+} = Sb^{3+}/In^{3+}/Bi^{3+}$, $X^{VII} = Cl^-/Br^-/I^-$), and $Cs_4M^{4+}B^{2+}{}_2X^{VII}{}_{12}$ ($M^{2+} = Ti^{2+}/V^{2+}/Cr^{2+}/Mn^{2+}/Fe^{2+}/Co^{2+}/Ni^{2+}$, $B^{2+} = Pb^{2+}/Ge^{2+}$, $X^{VII} = Cl^-/Br^-/I^-$) family compounds, in this work, we used the screened hybrid Heyd–Scuseria–Ernzerhof (HSE06) hybrid density functional[59,60] during the calculations of the band structures and the magnetic exchange parameters ($J_1$, $J_2$, and $J_3$) of the candidate compounds. The plane-wave cutoff energy of 400 eV was employed with the energy and force convergence criteria of $10^{-5}$ eV and 0.02 eV·Å$^{-1}$, respectively. DFT-D3 method was adopted for the van der Waals correction in all our calculations.[61] A 6 × 6 × 4 Γ-centered

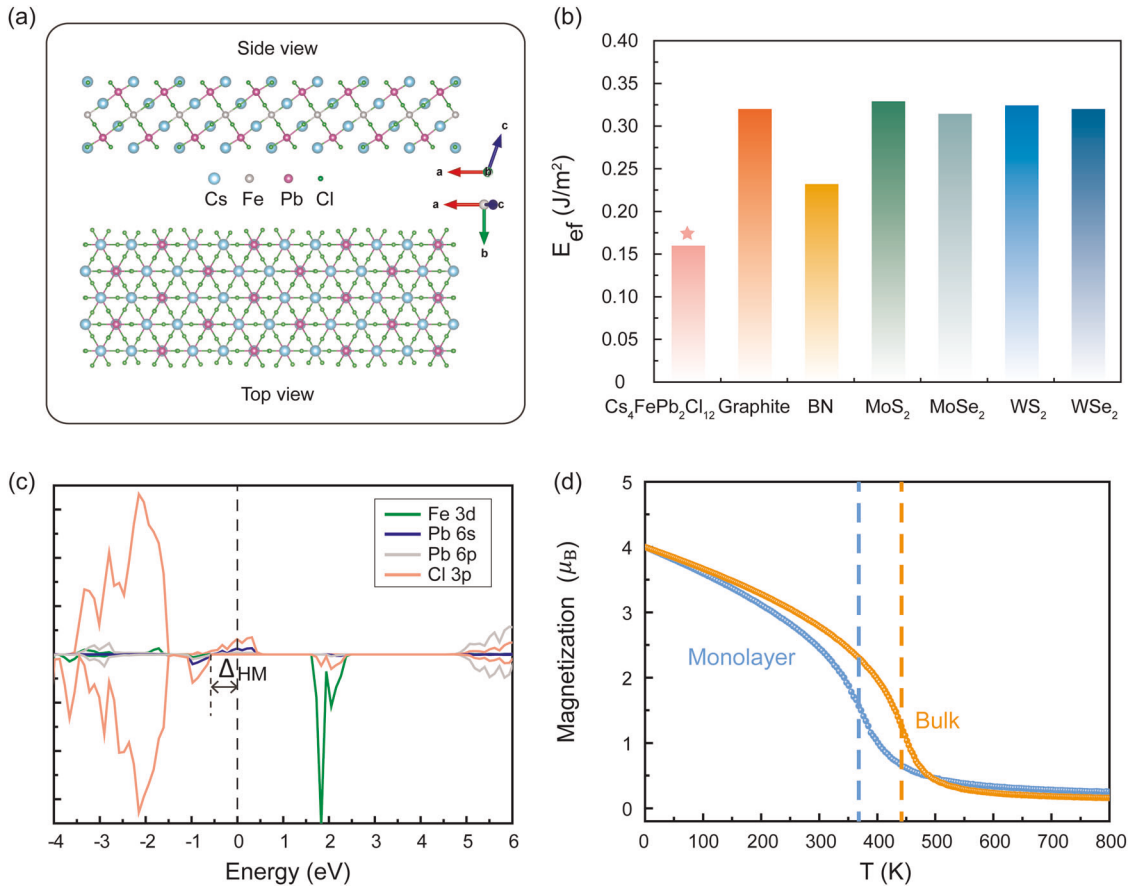


**Fig. 5** Magnetic properties of bulk and monolayer $Cs_4FePb_2Cl_{12}$. **a** Top and side views of $Cs_4FePb_2Cl_{12}$ monolayer. **b** Calculated exfoliation energy ($E_{ef}$) for $Cs_4FePb_2Cl_{12}$ and several layered compounds for comparison. **c** Orbital-projected DOS for $Cs_4FePb_2Cl_{12}$ monolayer. $E_f$ is set to zero. **d** Magnetic moment per Fe site as a function of temperature for bulk $Cs_4FePb_2Cl_{12}$ (orange line) and $Cs_4FePb_2Cl_{12}$ monolayer (blue line) from MC simulations. The vertical dashed lines indicate the $T_c$.

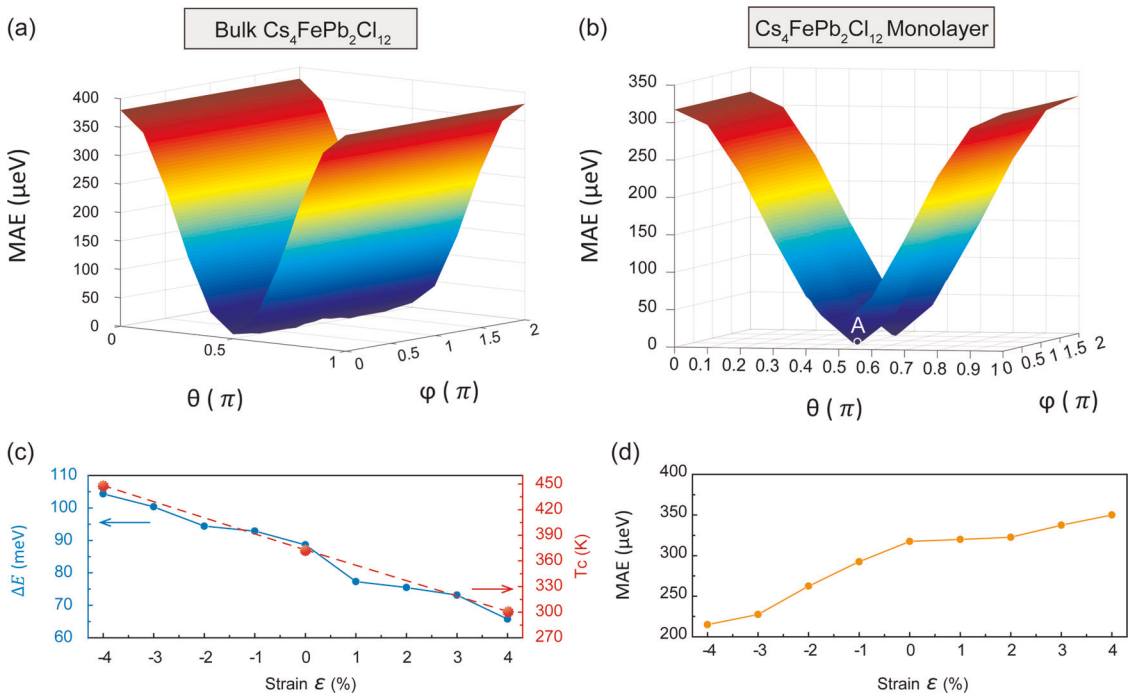


**Fig. 6** MAE and strain effects. Spatial (angular) dependence of MAE per unit cell (i.e., per Fe) for (**a**) bulk $Cs_4FePb_2Cl_{12}$ and (**b**) $Cs_4FePb_2Cl_{12}$ monolayer. Point A indicates the easy axis of magnetization. **c** Exchange energy ($\Delta E = E_{AFM} - E_{FM}$) and **d** MAE for $Cs_4FePb_2Cl_{12}$ monolayer as a function of in-plane (ab plane) biaxial strain ($\varepsilon$). Calculated $T_c$ for $Cs_4FePb_2Cl_{12}$ monolayer under −4% compressive strain and under 4% tensile strain from MC simulations are also shown in (**c**).

*k*-mesh was employed to sample the Brillouin zone of the primitive cell of $Cs_4M^{2+}B^{3+}{}_2X^{VII}{}_{12}$ and $Cs_4M^{4+}B^{2+}{}_2X^{VII}{}_{12}$ layered halide double perovskites. A sufficiently large vacuum region along the z direction of 14 Å was used in building $Cs_4FePb_2Cl_{12}$ monolayer.

### Phonon spectra and AIMD simulations

The phonon spectra were calculated by using the PHONOPY code[62] with the finite displacement method.[63] To verify the thermal stability of the selected materials, AIMD simulations were performed in the constant-volume and constant-temperature (*NVT*) ensemble at room temperature (300 K) by using the Nosé-Hoover thermostat.[64] The initial configurations of $Cs_4MnBi_2Cl_{12}$, $Cs_4CuBi_2Cl_{12}$, $Cs_4MnPb_2Cl_{12}$, $Cs_4MnPb_2Br_{12}$, and $Cs_4FePb_2Cl_{12}$ with 152 atoms (8 unit cells) were adopted. The time step was set to 1.0 fs.

### MAE calculations

To determine MAE, the spins are rotated to different directions, which are represented as function of the angles ($\theta$, $\phi$) in the spherical coordinate.[65] The SOC effect is taken into account. MAE is defined as the energy difference for the magnetization oriented along the easy-axis and along the hard-axis. The number of bands is set to be twice compared with the collinear calculation.

## DATA AVAILABILITY

The data generated or analyzed during this study are available from the corresponding authors upon reasonable request.

Received: 2 September 2019; Accepted: 5 November 2019;
Published online: 22 November 2019

## REFERENCES

1. Jourdan, M. et al. Direct observation of half-metallicity in the Heusler compound $Co_2MnSi$. *Nat. Commun.* **5**, 3974 (2014).
2. Wang, Q. et al. Large intrinsic anomalous Hall effect in half-metallic ferromagnet $Co_3Sn_2S_2$ with magnetic Weyl fermions. *Nat. Commun.* **9**, 3681 (2018).
3. Chen, W. T. et al. A half-metallic A- and B-site-ordered quadruple perovskite oxide $CaCu_3Fe_2Re_2O_{12}$ with large magnetization and a high transition temperature. *Nat. Commun.* **5**, 3909 (2014).
4. Hotta, K. et al. Atomic-layer alignment tuning for giant perpendicular magneto-crystalline anisotropy of 3d transition-metal thin films. *Phys. Rev. Lett.* **110**, 267206 (2013).
5. Alijani, V. et al. Quaternary half-metallic Heusler ferromagnets for spintronics applications. *Phys. Rev. B* **83**, 184428 (2011).
6. Kobayashi, K. I. et al. Room-temperature magnetoresistance in an oxide material with an ordered double-perovskite structure. *Nature* **395**, 677 (1998).
7. Xie, W.-H., Xu, Y.-Q., Liu, B.-G. & Pettifor, D. G. Half-metallic ferromagnetism and structural stability of zincblende phases of the transition-metal chalcogenides. *Phys. Rev. Lett.* **91**, 037204 (2003).
8. Li, X., Wu, X. & Yang, J. Room-temperature half-metallicity in La(Mn,Zn)AsO alloy via element substitutions. *J. Am. Chem. Soc.* **136**, 5664–5669 (2014).
9. Bessiere, A. et al. New thermal neutron scintillators: $Cs_2LiYCl_6$: $Ce^{3+}$ and $Cs_2LiYBr_6$: $Ce^{3+}$. *IEEE Trans. Nucl. Sci.* **51**, 2970–2972 (2004).
10. Milbrath, B. D., Peurrung, A. J., Bliss, M. & Weber, W. J. Radiation detector materials: An overview. *J. Mater. Res.* **23**, 2561–2581 (2011).
11. Glodo, J., Higgins, W. M., Loef, E. V. Dv & Shah, K. S. $Cs_2LiYCl_6$: Ce scintillator for nuclear monitoring applications. *IEEE Trans. Nucl. Sci.* **56**, 1257–1261 (2009).
12. Du, M.-H. & Biswas, K. Electronic structure engineering of elpasolites: Case of $Cs_2AgYCl_6$. *J. Lumines* **143**, 710–714 (2013).
13. Pan, W. et al. $Cs_2AgBiBr_6$ single-crystal X-ray detectors with a low detection limit. *Nat. Photonics* **11**, 726–732 (2017).
14. García de Arquer, F. P., Armin, A., Meredith, P. & Sargent, E. H. Solution-processed semiconductors for next-generation photodetectors. *Nat. Rev. Mat.* **2**, 16100 (2017).
15. Huang, J., Yuan, Y., Shao, Y. & Yan, Y. Understanding the physical properties of hybrid perovskites for photovoltaic applications. *Nat. Rev. Mat.* **2**, 17042 (2017).
16. Tang, G. et al. Layered halide double perovskites $Cs_{3+n}M(II)_nSb_2X_{9+3n}$ (M = Sn, Ge) for photovoltaic applications. *J. Phys. Chem. Lett.* **9**, 43–48 (2018).
17. Yantara, N. et al. Inorganic halide perovskites for efficient light-emitting diodes. *J. Phys. Chem. Lett.* **6**, 4360–4364 (2015).
18. Wang, Y. et al. All-inorganic colloidal perovskite quantum dots: a new class of lasing materials with favorable characteristics. *Adv. Mater.* **27**, 7101–7108 (2015).
19. Luo, J. et al. Efficient and stable emission of warm-white light from lead-free halide double perovskites. *Nature* **563**, 541–545 (2018).
20. Igbari, F., Wang, Z.-K. & Liao, L.-S. Progress of lead-free halide double perovskites. *Adv. Energy Mater.* **9**, 1803150 (2019).
21. Smith, M. D., Crace, E. J., Jaffe, A. & Karunadasa, H. I. The diversity of layered halide perovskites. *Ann. Rev. Mater. Res.* **48**, 111–136 (2018).
22. Xu, J. et al. Prediction of novel *p*-type transparent conductors in layered double perovskites: a first-principles study. *Adv. Funct. Mater.* **28**, 1800332 (2018).
23. Vargas, B. et al. A direct bandgap copper-antimony halide perovskite. *J. Am. Chem. Soc.* **139**, 9116–9119 (2017).
24. Vargas, B. et al. Optical, electronic, and magnetic engineering of <111> layered halide perovskites. *Chem. Mat.* **30**, 5315–5321 (2018).
25. Singhal, N., Chakraborty, R., Ghosh, P. & Nag, A. Low-bandgap $Cs_4CuSb_2Cl_{12}$ layered double perovskite: synthesis, reversible thermal changes, and magnetic interaction. *Chem. Asian J.* **13**, 2085–2092 (2018).
26. Wang, X. D. et al. The top-down synthesis of single-layered $Cs_4CuSb_2Cl_{12}$ halide perovskite nanocrystals for photoelectrochemical application. *Nanoscale* **11**, 5180–5187 (2019).
27. Zhao, X. G. et al. Design of lead-free inorganic halide perovskites for solar cells via cation-transmutation. *J. Am. Chem. Soc.* **139**, 2630–2638 (2017).
28. Kanamori, J. Superexchange interaction and symmetry properties of electron orbitals. *J. Phys. Chem. Solids* **10**, 87–98 (1959).
29. Goodenough, J. B. Theory of the role of covalence in the perovskite-type manganites [La, M(II)]$MnO_3$. *Phys. Rev.* **100**, 564–573 (1955).
30. Anderson, P. W. Antiferromagnetism. Theory oF Superexchange Interaction. *Phys. Rev.* **79**, 350–356 (1950).
31. Wang, H. P., Luo, W. & Xiang, H. J. Prediction of high-temperature quantum anomalous Hall effect in two-dimensional transition-metal oxides. *Phys. Rev. B* **95**, 125430 (2017).
32. Volonakis, G. et al. $Cs_2InAgCl_6$: a new lead-free halide double perovskite with direct band gap. *J. Phys. Chem. Lett.* **8**, 772–778 (2017).
33. Sun, Q. & Yin, W. J. Thermodynamic stability trend of cubic perovskites. *J. Am. Chem. Soc.* **139**, 14905–14908 (2017).
34. Li, C., Soh, K. C. K. & Wu, P. Formability of $ABO_3$ perovskites. *J. Alloy. Compd.* **372**, 40–48 (2004).
35. Belsky, A., Hellenbrandt, M., Karen, V. L. & Luksch, P. New developments in the Inorganic Crystal Structure Database (ICSD): accessibility in support of materials research and design. *Acta Crystallogr. Sect. B* **58**, 364–369 (2002).
36. Curtarolo, S. et al. AFLOW: an automatic framework for high-throughput materials discovery. *Comput. Mater. Sci.* **58**, 218–226 (2012).
37. Wang, X. et al. First-principles understanding of the electronic band structure of copper-antimony halide perovskite: the effect of magnetic ordering. arXiv preprint arXiv:1707.09539 (2017).
38. Dudarev, S. L. et al. Electron-energy-loss spectra and the structural stability of nickel oxide: an LSDA+U study. *Phys. Rev. B* **57**, 1505–1509 (1998).
39. Yao, K. L., Gao, G. Y., Liu, Z. L. & Zhu, L. Half-metallic ferromagnetism of zinc-blende CrS and CrP: a first-principles pseudopotential study. *Solid State Commun.* **133**, 301–304 (2005).
40. Xie, W.-H., Liu, B.-G. & Pettifor, D. G. Half-metallic ferromagnetism in transition metal pnictides and chalcogenides with wurtzite structure. *Phys. Rev. B* **68**, 134407 (2003).
41. Gao, G. Y. et al. Large half-metallic gaps in the quaternary Heusler alloys CoFeCrZ (Z=Al, Si, Ga, Ge): a first-principles study. *J. Alloy. Compd.* **551**, 539–543 (2013).
42. Bainsla, L. & Suresh, K. G. Equiatomic quaternary Heusler alloys: a material perspective for spintronic applications. *Appl. Phys. Rev.* **3**, 031101 (2016).
43. Huang, C. et al. Towards intrinsic room-temperature ferromagnetism in two-dimensional semiconductors. *J. Am. Chem. Soc.* **140**, 11519–11525 (2018).
44. Zhang, X. et al. High Curie temperature and intrinsic ferromagnetic half-metallicity in two-dimensional $Cr_3X_4$ (X = S, Se, Te) nanosheets. *Nanoscale Horiz.* **4**, 859–866 (2019).
45. Wang, B. et al. MnX (X = P, As) monolayers: a new type of two-dimensional intrinsic room temperature ferromagnetic half-metallic material with large magnetic anisotropy. *Nanoscale* **11**, 4204–4209 (2019).
46. Wang, B. et al. High Curie-temperature intrinsic ferromagnetism and hole doping-induced half-metallicity in two-dimensional scandium chlorine monolayers. *Nanoscale Horiz.* **3**, 551–555 (2018).
47. Miao, N. et al. 2D intrinsic ferromagnets from van der Waals antiferromagnets. *J. Am. Chem. Soc.* **140**, 2417–2420 (2018).
48. Bjorkman, T., Gulans, A., Krasheninnikov, A. V. & Nieminen, R. M. van der Waals bonding in layered compounds from advanced density-functional first-principles calculations. *Phys. Rev. Lett.* **108**, 235502 (2012).

49. Deng, Y. et al. Gate-tunable room-temperature ferromagnetism in two-dimensional $Fe_3GeTe_2$. *Nature* **563**, 94–99 (2018).
50. Samarth, N. Magnetism in flatland. *Nature* **546**, 216 (2017).
51. Gibertini, M., Koperski, M., Morpurgo, A. F. & Novoselov, K. S. Magnetic 2D materials and heterostructures. *Nat. Nanotechnol.* **14**, 408–419 (2019).
52. Bruno, P. Tight-binding approach to the orbital magnetic moment and magnetocrystalline anisotropy of transition-metal monolayers. *Phys. Rev. B* **39**, 865–868 (1989).
53. Ayaz Khan, S. et al. Magnetocrystalline anisotropy of FePt: a detailed view. *Phys. Rev. B* **94**, 144436 (2016).
54. Daalderop, G. H. O., Kelly, P. J. & Schuurmans, M. F. H. First-principles calculation of the magnetocrystalline anisotropy energy of iron, cobalt, and nickel. *Phys. Rev. B* **41**, 11919–11937 (1990).
55. Moulas, G. et al. High magnetic moments and anisotropies for $FexCo_{1-x}$ monolayers on Pt(111). *Phys. Rev. B* **78**, 214424 (2008).
56. Lehnert, A. et al. Magnetic anisotropy of Fe and Co ultrathin films deposited on Rh(111) and Pt(111) substrates: an experimental and first-principles investigation. *Phys. Rev. B* **82**, 094409 (2010).
57. Kresse, G. & Furthmüller, J. Efficient iterative schemes for ab initio total-energy calculations using a plane-wave basis set. *Phys. Rev. B* **54**, 11169–11186 (1996).
58. Perdew, J. P., Burke, K. & Ernzerhof, M. Generalized gradient approximation made simple. *Phys. Rev. Lett.* **77**, 3865–3868 (1996).
59. Heyd, J., Scuseria, G. E. & Ernzerhof, M. Hybrid functionals based on a screened Coulomb potential. *J. Chem. Phys.* **118**, 8207–8215 (2003).
60. Paier, J. et al. Screened hybrid density functionals applied to solids. *J. Chem. Phys.* **124**, 154709 (2006).
61. Lee, K. et al. Higher-accuracy van der Waals density functional. *Phys. Rev. B* **82**, 081101 (2010).
62. Togo, A., Oba, F. & Tanaka, I. First-principles calculations of the ferroelastic transition between rutile-type and $CaCl_2$-type $SiO_2$ at high pressures. *Phys. Rev. B* **78**, 134106 (2008).
63. Parlinski, K., Li, Z. Q. & Kawazoe, Y. First-principles determination of the soft mode in cubic $ZrO_2$. *Phys. Rev. Lett.* **78**, 4063–4066 (1997).
64. Nosé, S. A unified formulation of the constant temperature molecular dynamics methods. *J. Chem. Phys.* **81**, 511–519 (1984).
65. Chen, X. Z. et al. Antidamping-torque-induced switching in biaxial antiferromagnetic insulators. *Phys. Rev. Lett.* **120**, 207204 (2018).

## ACKNOWLEDGEMENTS

This work is supported by the National Key Research and Development Program of China (Grant Nos. 2017YFB0702401 and 2016YFB0700700), the Science Challenge Project (Grant Nos. TZ2016003, TZ2016004, and TZ2018004), the National Natural Science Foundation of China (Grant Nos. 51631005, 51571129, 11634003, and 11574024) and NSAF U1930402. C.X. and L.B. also thank the support of the Department of Energy, Office of Basic Energy Sciences, under Award No. DE-SC002220.

## AUTHOR CONTRIBUTIONS

J.X. and B.H. designed research; J.X. performed the DFT calculations; C.X. performed the MC calculations; J.X., C.X., J.-B.L., L.B., H.X., B.-X.L., and B.H. analyzed the data; and J.X., J.-B.L., H.X. and B.H. wrote the paper. All authors discussed and commented on the paper.

## COMPETING INTERESTS

The authors declare no competing interests.

## ADDITIONAL INFORMATION

**Supplementary information** is available for this paper at https://doi.org/10.1038/s41524-019-0252-6.

**Correspondence** and requests for materials should be addressed to J.-B.L. or B.H.

**Reprints and permission information** is available at http://www.nature.com/reprints

**Publisher's note** Springer Nature remains neutral with regard to jurisdictional claims in published maps and institutional affiliations.